Separation and Purification Technology 360 (2025) 131199

Contents lists available at ScienceDirect

Separation and Purification Technology

journal homepage: www.elsevier.com/locate/seppur

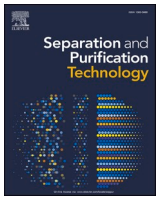

Tightly-bound interfaces between $ZnIn_2S_4$ nanosheets and few-layered Mo_2TiC_2 MXene induced highly efficient noble-metal-free Schottky junction for photocatalytic hydrogen evolution

Huihui Zhang, Yamei Huang, Xinglin Wang, Jiayi Meng, Linlin Gao, Yu Li, Yu Zhang, Yifan Liao, Wei-Lin Dai *

Department of Chemistry and Shanghai Key Laboratory of Molecular Catalysis and Innovative Materials, Fudan University, Shanghai 200433, PR China

ARTICLE INFO

Editor: Jorge Bedia

Keywords:
Tightly-bound interface
Few-layered Mo_2TiC_2 MXene
$ZnIn_2S_4$
Schottky junction
Photocatalytic hydrogen evolution

ABSTRACT

As a novel two-dimensional (2D) material with superior electrical conductivity, Mo_2TiC_2 MXene has been synthesized and applied in the fields of supercapacitors, lithium batteries, and electrocatalysis. Moreover, Mo_2TiC_2 MXene exhibits significant potential in photocatalytic processes due to its excellent light absorption and electron acceptance properties. Consequently, a few-layered Mo_2TiC_2 MXene with a large lamellar structure was designed and synthesized using etching and intercalation methods. Based on this, a tightly-bound $ZnIn_2S_4/Mo_2TiC_2$ binary composite was then fabricated through an in situ solvothermal process. Under simulated sunlight irradiation, the optimal $ZnIn_2S_4$/10 %Mo_2TiC_2 composite exhibited an outstanding photocatalytic hydrogen evolution (PHE) rate of 4.3 mmol·g^{-1}·h^{-1} (using 10 mg of catalyst), which was 3.8 times higher than that of $ZnIn_2S_4$ and also surpassed the activity of $ZnIn_2S_4$ with 1 % Pt as co-catalyst. According to in situ X-ray photoelectron spectroscopy (XPS) and density functional theory (DFT) calculations, the enhanced PHE activity was attributed to the formation of a Schottky junction with the tightly-bound interface between $ZnIn_2S_4$ and Mo_2TiC_2, which effectively facilitated the transfer of photogenerated electrons and inhibited electron recombination in the composites. Additionally, all the composites showed improved light absorption intensity compared to pure $ZnIn_2S_4$, which also contributed to the enhanced PHE performance. This work demonstrated the superior activity of few-layered Mo_2TiC_2 MXene as a noble-metal-free co-catalyst, and its large lamellar structure made it an ideal substrate for further incorporating with other semiconductors to construct high-performance MXene-based heterostructures.

1. Introduction

As a sustainable green energy source with high energy density, hydrogen (H_2) has been regarded as an ideal energy carrier for replacing fossil fuels [1–3]. Since the first report on TiO_2 as an electrode for electro-photocatalytic water splitting in 1972 [4], the photocatalytic hydrogen evolution (PHE) process has attracted significant research interest as a clean and effective method. In recent years, lots of semiconductors have been utilized as highly-efficient photocatalysts in the PHE process, including metal oxides [5–7], metal sulfides [8–11], g-C_3N_4 [12–14], metal nitrides [15,16], metal selenides [17–19], metal–organic-frameworks (MOF) [20–23] and covalent-organic-frameworks (COF) [24,25]. Among these materials, $ZnIn_2S_4$ stands out as an excellent photocatalyst as a result of its appropriate band gap, superior chemical stability and robust visible-light absorption capability [26–28]. However, the photocatalytic performance of pristine $ZnIn_2S_4$ is largely hindered by the rapid recombination of photogenerated charge carriers. Therefore, lots of strategies have been employed to enhance its photocatalytic activity, such as introducing sulfur or oxygen vacancies [29,30], doping elements [31], and fabricating heterostructures [32–35]. Notably, the incorporation of co-catalysts is an effective strategy for accelerating charge carriers transfer and separation in $ZnIn_2S_4$, thereby significantly enhancing its photocatalytic activity. Additionally, noble-metal-free co-catalysts are emerging as promising alternatives to traditional noble metals due to their low cost [36–38].

Recently, as a novel 2D material with high electrical conductivity and strong electron acceptance capability, MXene has been widely applied in various fields, including supercapacitors [39], lithium batteries [40], electrocatalysis [41–44] and photocatalysis [45–47]. For instance, Ti_3C_2 MXene, a typical MXene, has been widely reported as an

* Corresponding author.
E-mail address: wldai@fudan.edu.cn (W.-L. Dai).

https://doi.org/10.1016/j.seppur.2024.131199
Received 3 November 2024; Received in revised form 13 December 2024; Accepted 18 December 2024
Available online 19 December 2024

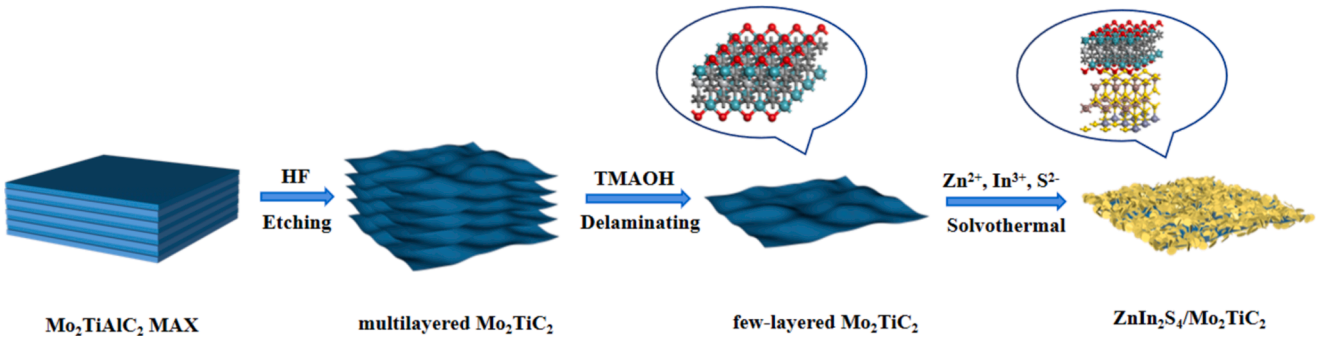

Scheme 1. Schematic illustration of the synthesis route of $ZnIn_2S_4/Mo_2TiC_2$ composites.

effective co-catalyst in photocatalytic processes [48–51]. More recently, Mo_2TiC_2 MXene has been successfully synthesized and used as a bimetallic MXene, further expanding the range and application of MXene materials. However, the crystal phase and morphology of the prepared Mo_2TiC_2 MXene remain unsatisfactory, as reported in some studies [52,53], which hinders its integration with other semiconductor materials as a platform. Furthermore, to our knowledge, the application of few-layered Mo_2TiC_2 MXene in PHE process remains limited. Besides, it is worth noting that the strong interfacial interaction between the components is important for the charge transfer performance and photocatalytic activity of the heterojunctions as many previous reports have illustrated [35,54,55].

In this work, we synthesized a few-layered Mo_2TiC_2 MXene with a large lamellar structure by modifying the synthetic method. Then, we fabricated tightly-bound $ZnIn_2S_4/Mo_2TiC_2$ binary composites via an in situ solvothermal process for the PHE reaction. Under simulated sunlight irradiation, $ZnIn_2S_4$/10 %Mo_2TiC_2 composite achieved the maximum H_2 evolution rate of 4.3 mmol·g^{-1}·h^{-1} (using 10 mg of catalyst), which was 3.8 times higher than that of bare $ZnIn_2S_4$ and even surpassed the performance of $ZnIn_2S_4$ with 1 % Pt as a co-catalyst. Based on the in situ XPS and DFT calculation results, it was deduced that the Schottky junction formed between $ZnIn_2S_4$ and Mo_2TiC_2 accelerated the photogenerated charge carriers transfer and inhibited the electrons backflow within the composites. Moreover, the tightly-bound interface between $ZnIn_2S_4$ nanosheets and few-layered Mo_2TiC_2 MXene was beneficial for shortening the transfer path of electrons, thereby enhancing the PHE activity of the composites. This work demonstrated the significant application potential of few-layered Mo_2TiC_2 MXene as an effective, noble-metal-free co-catalyst in the process of photocatalytic water splitting.

2. Experimental

2.1. Preparation of few-layered Mo_2TiC_2 MXene nanosheets

Mo_2TiC_2 MXene nanosheets were synthesized using a wet chemical etching method and an intercalation process with tetramethylammonium hydroxide (TMAOH), as previously reported with some modifications [45]. In detail, 2.0 g of Mo_2TiAlC_2 MAX powder was slowly added into 40 mL of hydrogen fluoride (HF, 40 %), and the mixture was stirred at 55 °C for 48 h to etch out Al layers. After natural cooling, the obtained slurry was washed with deionized (DI) water and centrifuged at 10,000 rpm several times until the pH of the supernatant was approximately 6. The multilayered Mo_2TiC_2 MXene powder was then collected after freeze-drying and designated as M−Mo_2TiC_2. Next, 375 mg of M−Mo_2TiC_2 was dispersed in 10 mL of 2.5 % TMAOH aqueous solution, which was prepared by diluting the 25 % TMAOH aqueous solution. After being stirred for 12 h, the mixture was washed with DI water and centrifuged at 10,000 rpm several times until the pH of the supernatant reached approximately 7. Then, the resulting sediment was added to 50 mL of DI water and sonicated for 1 h under the argon atmosphere, followed by centrifugation at 3,500 rpm for additional 0.5 h. The supernatant was then collected and freeze-dried to obtain the few-layered Mo_2TiC_2 MXene nanosheets, which was labeled as Mo_2TiC_2.

2.2. Preparation of $ZnIn_2S_4$ nanosheets/few-layered Mo_2TiC_2 MXene nanosheets ($ZnIn_2S_4/Mo_2TiC_2$)

The binary composites with varying amounts of few-layered Mo_2TiC_2 nanosheets were prepared by in situ solvothermal method, with some adjustments based on our previous work [56]. Specifically, taking $ZnIn_2S_4$/10 %Mo_2TiC_2 sample as an example, 13 mg of Mo_2TiC_2 MXene was added to a mixture of 16 mL of DI water and 4 mL of glycerol. After complete dispersion, 326 mg of zinc chloride ($ZnCl_2$), 702 mg of indium chloride tetrahydrate ($InCl_3·4H_2O$) and 360 mg of thioacetamide (TAA) were sequentially introduced into the above mixture. The solution was stirred for additional 0.5 h, then kept at 80 °C for 1.5 h with continuous stirring. Upon natural cooling, the resulting precipitate was isolated by centrifugation, washed with DI water and ethanol, and then freeze-dried overnight to obtain $ZnIn_2S_4$/10 %Mo_2TiC_2 sample. For comparison, binary composites were prepared by adding varying amounts of Mo_2TiC_2 powder, and the resulting samples were labeled as $ZnIn_2S_4$/x %Mo_2TiC_2, where x % was the mass ratio of added Mo_2TiC_2 in the binary composites. In addition, $ZnIn_2S_4$ was prepared by the same procedure without the addition of Mo_2TiC_2.

2.3. Preparation of comparative samples

The $ZnIn_2S_4$/10 %M−Mo_2TiC_2 binary composite was prepared via the same in situ solvothermal process by adding 13 mg of M−Mo_2TiC_2 instead of Mo_2TiC_2, and the sample constructed by mechanically mixing Mo_2TiC_2 and $ZnIn_2S_4$ was named as M−$ZnIn_2S_4$/10 %Mo_2TiC_2. In addition, $ZnIn_2S_4$/10 %Ti_3C_2 was synthesized by the same solvothermal process with 13 mg of few-layered Ti_3C_2 MXene powder, which was obtained by the method described in our previous work [17], instead of Mo_2TiC_2.

3. Results and discussion

3.1. Morphology and structure characterization

The preparation of $ZnIn_2S_4/Mo_2TiC_2$ binary composites was briefly described in Scheme 1. Firstly, the Al layers in Mo_2TiAlC_2 MAX were etched using an aqueous solution of HF to form multilayered Mo_2TiC_2 MXene. Subsequently, few-layered Mo_2TiC_2 MXene nanosheets were obtained through an intercalation process with TMAOH, followed by delamination via ultrasonication. Finally, $ZnIn_2S_4$ nanosheets were evenly anchored on few-layered Mo_2TiC_2 MXene nanosheets, forming the tightly-bound binary composites by in situ solvothermal process.

The microstructure and morphology of the samples were characterized using scanning electron microscopy (SEM) and field-emission transmission electron microscopy (FE-TEM). For convenience, the microstructure of $ZnIn_2S_4$/50 %Mo_2TiC_2 was investigated rather than

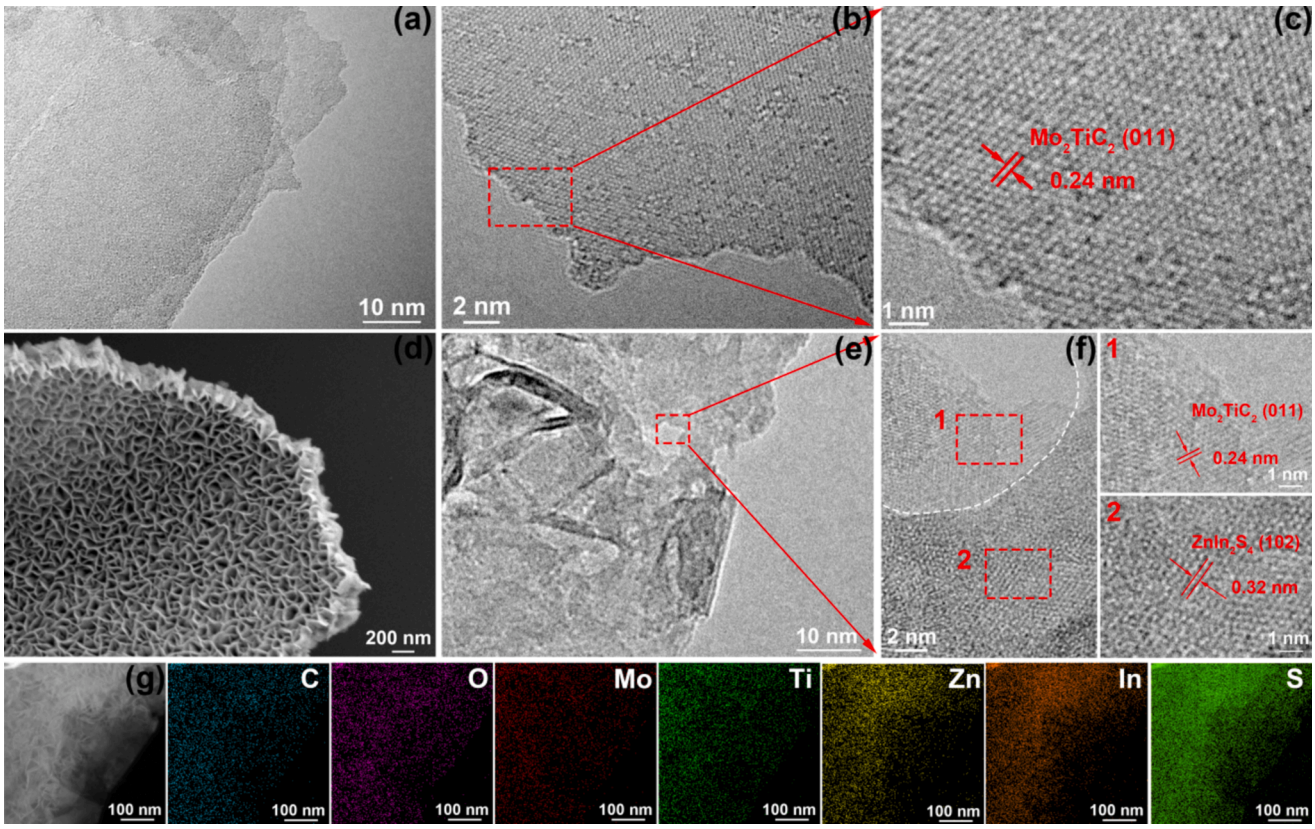

Fig. 1. TEM image (a), HRTEM image (b) and enlarged HRTEM image (c) of Mo_2TiC_2, SEM image (d), TEM image (e) and HRTEM image (f) of $ZnIn_2S_4$/50 %Mo_2TiC_2 , the marked 1, 2 rectangles represent Mo_2TiC_2 and $ZnIn_2S_4$, (g) HAADF image and element mappings of C, O, Mo, Ti, Zn, In and S in $ZnIn_2S_4$/50 %Mo_2TiC_2.

that of $ZnIn_2S_4$/10 %Mo_2TiC_2. As shown in Fig. S1, M−Mo_2TiC_2 exhibited a large lamellar structure composed of numerous stacked nanosheets. After the intercalation and delamination processes, the resulting Mo_2TiC_2 displayed a large lamellar morphology with fewer stacked nanosheets compared to M−Mo_2TiC_2 (Fig. 1a), which was beneficial for its close integration with $ZnIn_2S_4$. Moreover, the thicknesses of M−Mo_2TiC_2 and few-layered Mo_2TiC_2 nanosheets were examined, and the corresponding atomic force microscopy (AFM) images and height profiles were described in Fig. S2 and Fig. S3, respectively. It was clear that the thickness of M−Mo_2TiC_2 was above 100 nm, whereas the thickness of few-layered Mo_2TiC_2 nanosheets was less than 1.80 nm, further confirming the few-layered structure of Mo_2TiC_2 MXene [17]. As depicted in Fig. 1b and 1c, the lattice spacing of 0.24 nm corresponded to the (011) crystal plane of Mo_2TiC_2, which was consistent with the previous report [57]. In addition, pristine $ZnIn_2S_4$ exhibited a microsphere morphology, formed by the aggregation of nanosheets (Fig. S4). As shown in Fig. 1d-e, $ZnIn_2S_4$ nanosheets uniformly grown on the surface of Mo_2TiC_2 nanosheets in $ZnIn_2S_4$/50 % Mo_2TiC_2 composite, forming a closely integrated hierarchical structure with the tightly-bound interface, which could effectively reduce the charge transfer distance and enhance the charge transfer efficiency. Furthermore, as described in Fig. 1f, the high-resolution transmission electron microscopy (HRTEM) result revealed the clear boundary between $ZnIn_2S_4$ and Mo_2TiC_2 in the composite, and the lattice distances of 0.24 nm and 0.32 nm were assigned to the (011) plane of Mo_2TiC_2 and the (102) plane of $ZnIn_2S_4$, respectively, further implied the tightly-bound interface in the fabricated binary composite. Moreover, the elemental mapping results displayed in Fig. 1g indicated that Zn, In, S, Mo, Ti, C and O were uniformly distributed throughout the composite, collectively convinced the successful preparation of the binary composite, in which $ZnIn_2S_4$ nanosheets evenly dispersed on the surface of few-layered Mo_2TiC_2 MXene nanosheets.

X-ray diffraction (XRD) patterns were utilized to analyze the crystal structure of the prepared samples. As shown in Fig. 2a, the characteristic diffraction peaks of Mo_2TiAlC_2 MAX were consistent with the standard card (JCPDS, NO. 89–4897), and the main peaks at 9.4°, 19.0°, 28.6°, 34.9° and 39.6° were related to (002), (004), (006), (101) and (104) planes. Compared with Mo_2TiAlC_2 MAX, (002), (004) and (006) diffraction peaks of M−Mo_2TiC_2 shifted to lower angles at 5.8°, 11.8° and 17.6°, implying the removal of Al layers and the successful synthesis of M−Mo_2TiC_2 [39]. At the same time, it could be noticed that M−Mo_2TiC_2 exhibited some weak peaks in the range of 35-45°, which was mainly due to the presence of residual MAX precursor. After the intercalation process, the obtained Mo_2TiC_2 showed more intense peaks than M−Mo_2TiC_2, with no obvious peaks in the range of 35-45°, the results jointly demonstrated the more ordered structure and higher crystallinity of Mo_2TiC_2. As shown in Fig. 2b, the diffraction peaks at 21.6°, 27.7° and 47.2° corresponded to (006), (102) and (110) planes of the hexagonal $ZnIn_2S_4$ (JCPDS, NO. 65–2023) [26]. Moreover, the XRD patterns of the $ZnIn_2S_4$/Mo_2TiC_2 binary heterojunctions were consistent with that of $ZnIn_2S_4$, with no discernible diffraction peaks of Mo_2TiC_2, which was primarily attributed to the relatively weak diffraction intensity and the uniform dispersion of Mo_2TiC_2 within the composites [58]. For further confirming the composition and molecular structure of the catalysts, Fourier-transform infrared spectroscopy (FT-IR) was analyzed, as shown in Fig. S5a, all samples exhibited a strong peak at 3460 cm^{-1}, which was associated with the physically adsorbed water molecules on the surface. Additionally, as for the pristine $ZnIn_2S_4$, the obvious peaks at 1630 and 1020 cm^{-1} were related to the N–H scissoring and C–H stretching vibration, respectively, which might due to the residual TAA in the synthesized sample [9]. Furthermore, FT-IR spectra of $ZnIn_2S_4$/Mo_2TiC_2 composites were almost consistent with the pristine $ZnIn_2S_4$, as a result of the low content and high dispersion of Mo_2TiC_2 in the composites [17]. Raman spectra were also tested to explore the

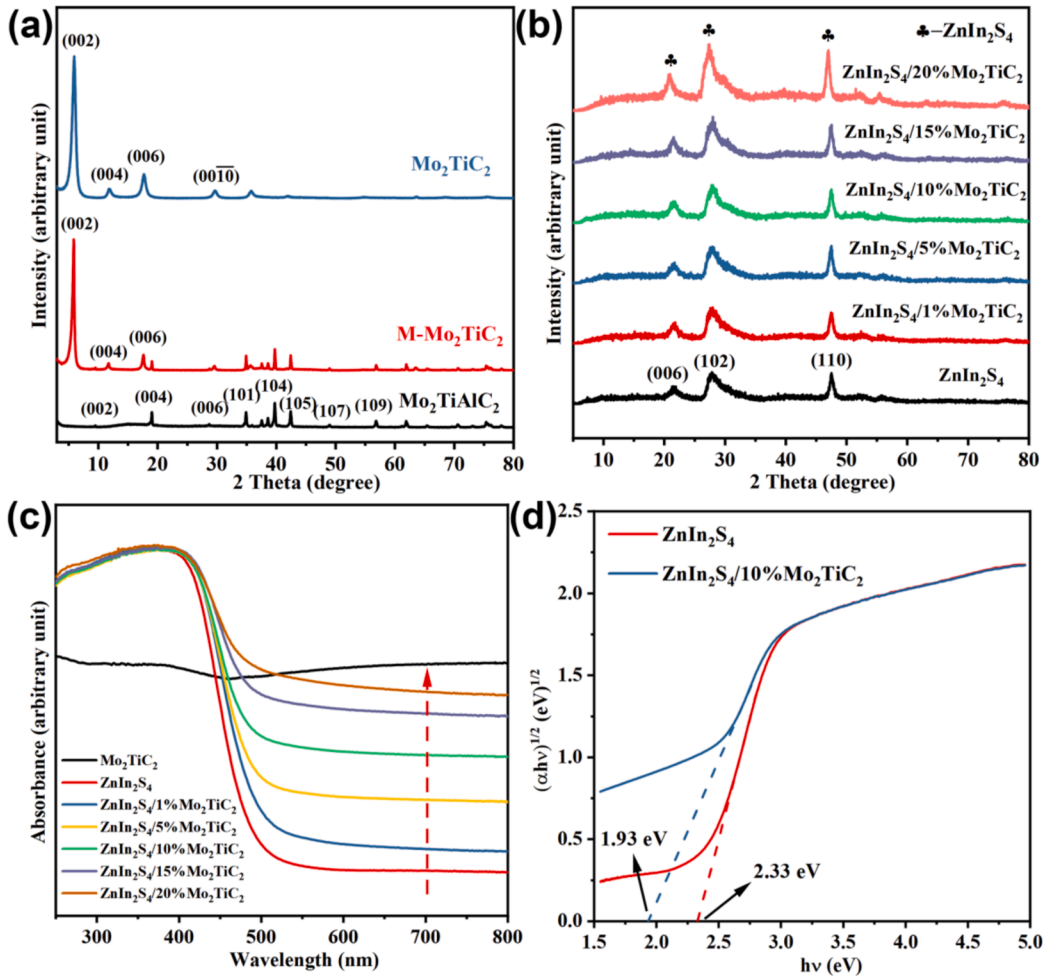

Fig. 2. (a) XRD patterns of Mo_2TiAlC_2, M–Mo_2TiC_2, Mo_2TiC_2, XRD patterns (b) and UV–vis. DRS spectra (c) of the prepared samples, (d) Tauc plots of $ZnIn_2S_4$ and $ZnIn_2S_4$/10 %Mo_2TiC_2.

molecular structure of the catalysts, as described in Fig. S5b, in the case of pristine Mo_2TiC_2, the peaks at 285, 822 and 994 cm^{-1} were attributed to the O = Mo bending, O-Mo_2 and O = Mo stretching, as reported previously [41], which further confirmed the fabrication of Mo_2TiC_2. In addition, the Raman spectrum of pristine $ZnIn_2S_4$ showed two obvious peaks at 250 and 365 cm^{-1} [45,46], and all binary composites exhibited similar Raman spectra with pristine $ZnIn_2S_4$ (Fig. S5c), which was also due to the low content of Mo_2TiC_2 in the composites.

As displayed in Fig. 2c, the optical absorption property of the obtained samples was explored by UV–vis diffuse reflectance spectra (UV–vis. DRS), and the color of the samples was displayed in Fig. S6. It was evident that pristine $ZnIn_2S_4$ displayed limited visible light response capability, with an absorption edge at around 500 nm. In contrast, $ZnIn_2S_4/Mo_2TiC_2$ binary composites exhibited enhanced light absorption intensity in the visible region as the content of Mo_2TiC_2 increased, which was owing to the excellent light absorption of black Mo_2TiC_2 across the full spectrum, and the gradually increased light absorption intensity of $ZnIn_2S_4/Mo_2TiC_2$ composites was consistent with the color change from light yellow to dark green. The improved light absorption activity of the binary composites was conducive to the PHE process. Additionally, the band gap energies (E_g) of $ZnIn_2S_4$ and $ZnIn_2S_4$/10 % Mo_2TiC_2 were calculated as 2.33 and 1.93 eV, respectively, using the Kubelka-Munk transformation formula (Fig. 2d).

In addition, the specific surface area and pore size distribution of the samples were measured using nitrogen (N_2) adsorption–desorption isotherms. As shown in Fig. S7a, the specific surface area of pristine Mo_2TiC_2 was determined to be 4 m^2/g, indicating its poor porosity. Meanwhile, both pure $ZnIn_2S_4$ and $ZnIn_2S_4$/10 %Mo_2TiC_2 exhibited typical reversible type-IV isotherms, suggesting the presence of mesoporous structure, and the mesoporous structure could provide direct pathway for the diffusion of reactants and products, such as water molecules and hydrogen gas, ensuring that more reactive species could reach the catalytic sites efficiently [48]. Notably, $ZnIn_2S_4$/10 %Mo_2TiC_2 showed a slightly reduced specific surface area of 46 m^2/g compared to that of $ZnIn_2S_4$ (52 m^2/g), evaluated by the Brunauer-Emmett-Teller (BET) model (Fig. S7b-c). This result was primarily due to the surface coverage and pore blockage caused by the integration of Mo_2TiC_2 nanosheets, which also lead to the slight reduction of pore volume of $ZnIn_2S_4$/10 %Mo_2TiC_2 as shown in Table. S1. Therefore, it could be concluded that the specific surface area was not the primary determinant of the photocatalytic performance in $ZnIn_2S_4/Mo_2TiC_2$ heterojunction system. Despite the specific surface area reduction, $ZnIn_2S_4$/10 %Mo_2TiC_2 still exhibited improved photocatalytic performance, mainly due to the enhanced charge transfer efficiency and light absorption property formed by the tightly-bound interface between $ZnIn_2S_4$ and Mo_2TiC_2. Furthermore, the pore size distribution of the samples was illustrated in Fig. S7d-f, revealing that the average pore width of $ZnIn_2S_4$/10 %Mo_2TiC_2 was similar to that of pure $ZnIn_2S_4$.

X-ray photoelectron spectroscopy (XPS) was an effective method for exploring the surface composition and chemical state of the samples. For convenience, $ZnIn_2S_4$/50 %Mo_2TiC_2 was analyzed instead of $ZnIn_2S_4$/10 %Mo_2TiC_2 binary composite. The full survey spectra in Fig. 3a indicated the existence of Mo, Ti, C and O elements in Mo_2TiC_2 and Zn, In and S elements in $ZnIn_2S_4$, suggesting the successful synthesis of pure

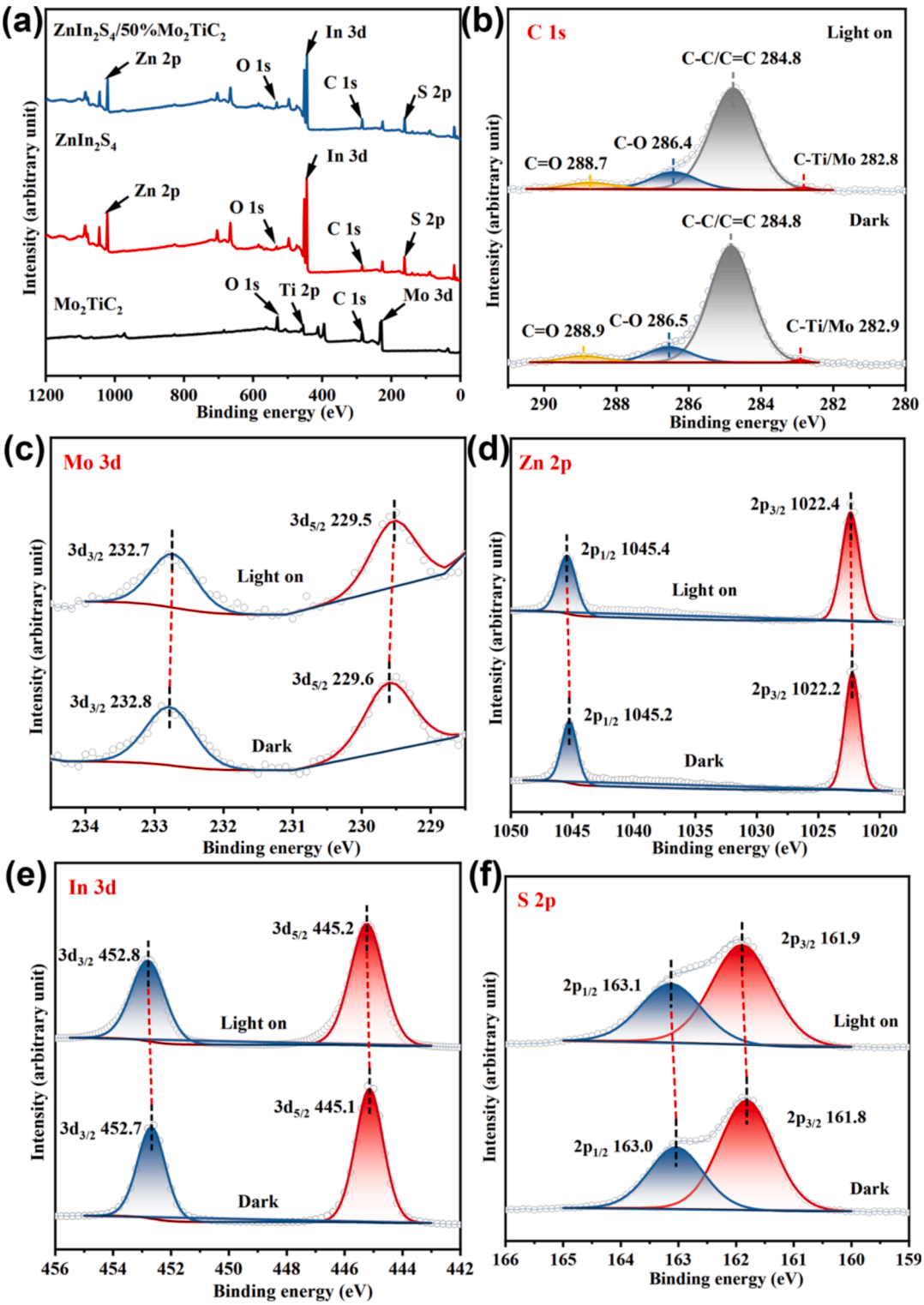

Fig. 3. (a) XPS survey spectra of the comparative samples, in situ C 1s XPS spectra (b), Mo 3d XPS spectra (c), Zn 2p XPS spectra (d), In 3d XPS spectra (e) and S 2p XPS spectra (f) of $ZnIn_2S_4$/50 %Mo_2TiC_2 (Dark and Light on).

Mo_2TiC_2 and $ZnIn_2S_4$. However, Mo and Ti elements were not observed in the full spectrum of $ZnIn_2S_4$/50 %Mo_2TiC_2 composite, primarily because the surface of the few-layered Mo_2TiC_2 nanosheets was entirely covered by $ZnIn_2S_4$. Additionally, the binding energy positions of Mo 3d and Ti 2p were close to those of S 2 s and In 3d, which jointly contributed to the non-detectability of Mo and Ti elements in the composite. As illustrated in Fig. S8a, C 1 s XPS spectrum of pristine Mo_2TiC_2 could be divided into four peaks corresponding to the bonds of C-Ti/Mo, C–C/C=C, C-O and C=O, respectively. Mo 3d spectrum of Mo_2TiC_2 exhibited two peaks located at 229.4 and 232.6 eV, which were attributed to $Mo3d_{5/2}$ and $Mo3d_{3/2}$ (Fig. S8b). Furthermore, the peaks centered at 455.7 and 461.6 eV in Ti 2p spectrum of Mo_2TiC_2 were attributed to Ti-C bond, and the other two peaks at 457.7 and 463.4 eV were identified as the satellite peaks of Ti-C bond (Fig. S8c). As displayed in Fig. S8d-f, the

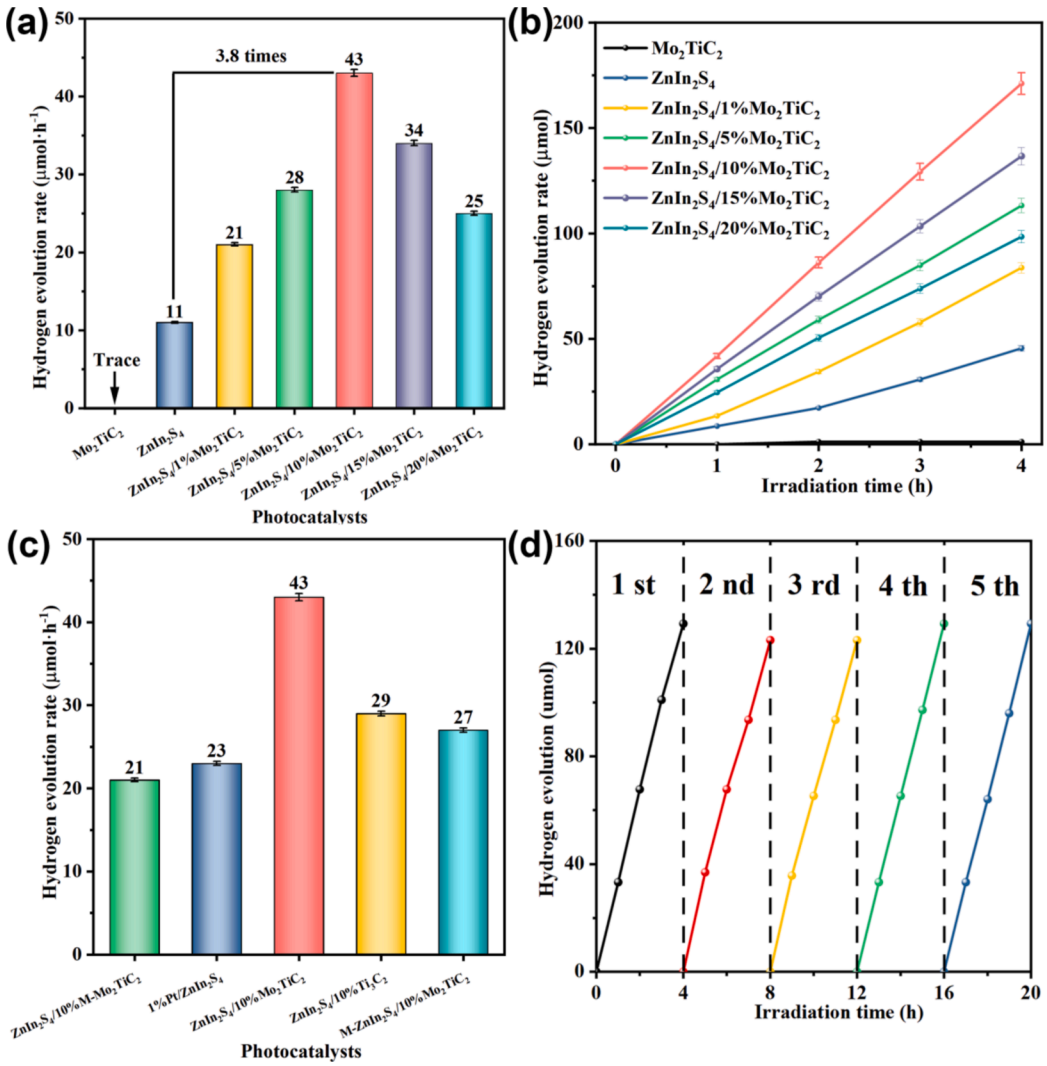

Fig. 4. (a-c) Photocatalytic H_2 evolution activity of the as-obtained catalysts, all data was obtained by four times repeat experiments, (d) recycling H_2 evolution test of $ZnIn_2S_4$/10 %Mo_2TiC_2.

binding energies of 1022.2 and 1045.3 eV were assigned to Zn^{2+} in $ZnIn_2S_4$, and In 3d spectrum of $ZnIn_2S_4$ was divided into two peaks at 452.6 and 445.1 eV, corresponding to In $3d_{3/2}$ and In $3d_{5/2}$, respectively. Additionally, the binding energies of 161.7 and 162.9 eV were assigned to S^{2-} in $ZnIn_2S_4$. Besides, in situ light irradiation XPS spectra were carried out to investigate the charge transfer behavior in $ZnIn_2S_4$/Mo_2TiC_2 composite. As displayed in Fig. 3b, the binding energy of the peak of C-Ti/Mo bond in $ZnIn_2S_4$/50 %Mo_2TiC_2 composite shifted negatively under light irradiation compared to that of dark condition. Meanwhile, it could be observed that the binding energy of Mo 3d peaks also shifted negatively under light irradiation (Fig. 3c). And the peaks corresponding to Zn 2p, In 3d and S 2p in the binary composite all shifted to higher binding energies after exposure to light, as described in Fig. 3d-f. This shift indicated that the photogenerated charge transferred from $ZnIn_2S_4$ to Mo_2TiC_2 within the heterojunction under illumination.

3.2. Photocatalytic hydrogen evolution activity

The photocatalytic hydrogen production performance of the synthesized catalysts was evaluated using Na_2S and Na_2SO_3 as sacrificial agents, without the addition of any co-catalyst. As shown in Fig. 4a, the pure Mo_2TiC_2 exhibited almost no H_2 production activity due to its metallic property, and $ZnIn_2S_4$ exhibited a moderate H_2 evolution rate of 1.1 mmol·g^{-1}·h^{-1} (using 10 mg of catalyst), as a result of its limited light absorption ability and severe photogenerated charge carrier recombination. After combining with few-layered Mo_2TiC_2 nanosheets, all binary composites synthesized via in situ solvothermal process showed significantly accelerated PHE rates, mainly attributed to the formation of Schottky heterojunction with improved light absorption ability and accelerated charge transfer efficiency. In particular, $ZnIn_2S_4$/10 %Mo_2TiC_2 exhibited the optimal H_2 evolution rate of 4.3 mmol·g^{-1}·h^{-1}, which was 3.8 times higher than that of bare $ZnIn_2S_4$. Besides, the optimal H_2 evolution performance of $ZnIn_2S_4$/10 %Mo_2TiC_2 was superior to those of many $ZnIn_2S_4$-based photocatalysts previously reported, as described in Table S2. Meanwhile, the H_2 production amount of all samples increased linearly with the irradiation time (Fig. 4b), indicating their excellent photostability. Moreover, as displayed in Fig. 4c, $ZnIn_2S_4$/10 %Mo_2TiC_2 exhibited an obviously higher PHE rate compared to $ZnIn_2S_4$/10 %M−Mo_2TiC_2 (2.1 mmol·g^{-1}·h^{-1}) and M−$ZnIn_2S_4$/10 %Mo_2TiC_2 (2.7 mmol·g^{-1}·h^{-1}), confirming that the strong interfacial interaction induced by the tight-bound interface between $ZnIn_2S_4$ and Mo_2TiC_2 was crucial for the improved photocatalytic performance of the binary composite. Specifically, the PHE efficiency of $ZnIn_2S_4$/10 %Mo_2TiC_2 also surpassed those of $ZnIn_2S_4$ with 10 %Ti_3C_2 or 1 %Pt as co-catalysts, suggesting the excellent co-catalytic effect of the few-layered Mo_2TiC_2 nanosheets. Besides, the photocatalytic stability was an important property of catalysts, as depicted in Fig. 4d, $ZnIn_2S_4$/10 %Mo_2TiC_2 catalyst maintained a steady H_2 release rate over

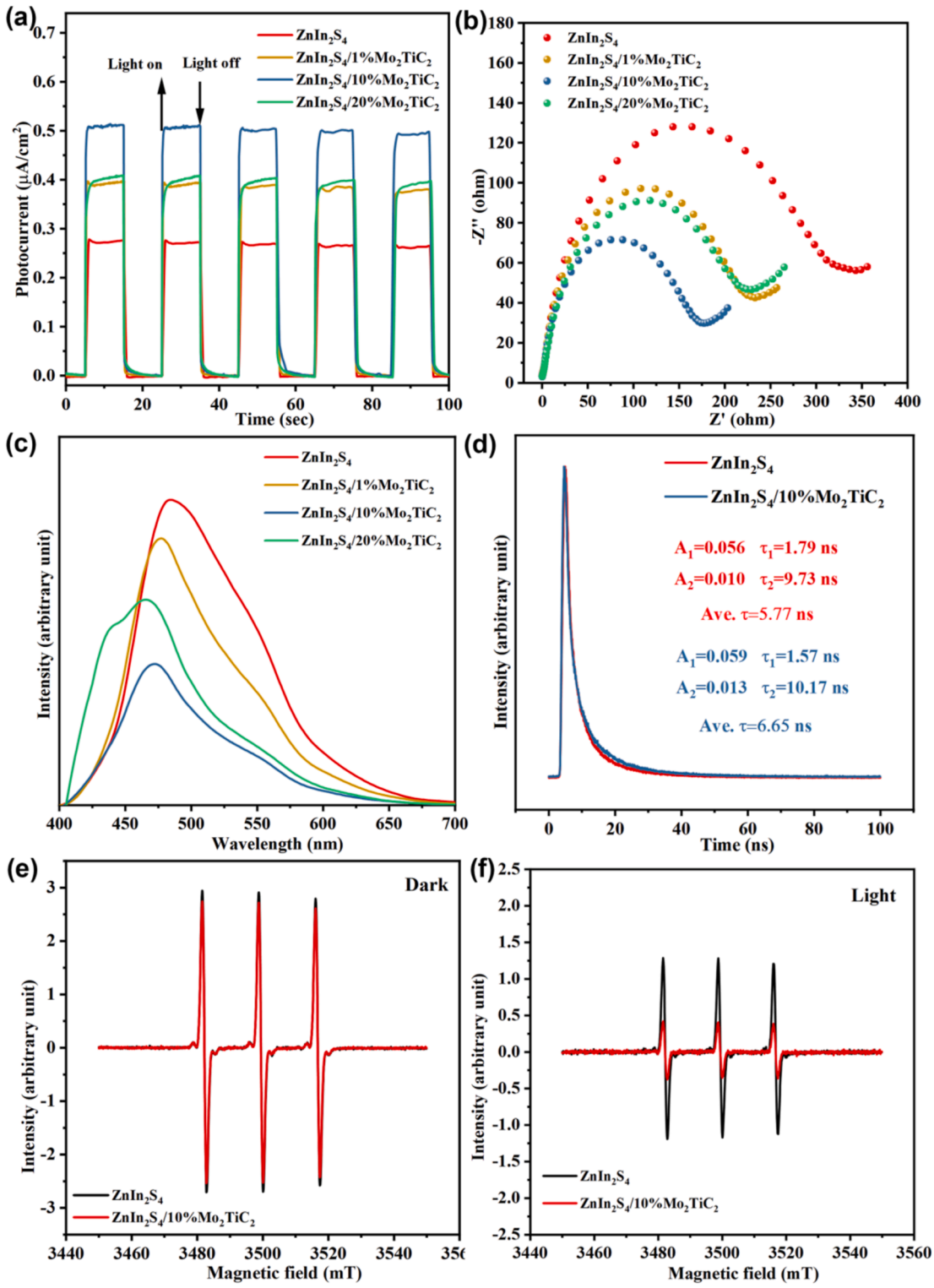

Fig. 5. Transient photocurrent response (a), electrochemical impedance spectra (EIS) (b), photoluminescence (PL) spectra (c) and time-resolved photoluminescence (TRPL) spectra (d) of $ZnIn_2S_4$ and composites, TEMPO spin-trapping ESR spectra of $ZnIn_2S_4$ and $ZnIn_2S_4$/10 %Mo_2TiC_2 in the dark (e) and under light (f).

five cycles. XRD and SEM results in Fig. S9 implied that the crystal structure and morphology of the catalyst were maintained after the cycling test, demonstrating its excellent stability during the photocatalytic process. For comparison, the PHE performance of $ZnIn_2S_4$/10 %Mo_2TiC_2 was also tested in other sacrificial agent systems (Fig. S10a), and Na_2S-Na_2SO_3 was identified as the optimal sacrificial agent for the photocatalyst, primarily due to its lower permittivity and higher oxidation potential [59]. The apparent quantum efficiency (AQE) of $ZnIn_2S_4$/10 %Mo_2TiC_2 was measured under similar conditions with irradiation lights of different wavelengths. As shown in Fig. S10b, the AQE reached up to 0.75 % at 350 nm, with detailed results provided in Table S3. In conclusion, these findings confirmed that $ZnIn_2S_4$/10 %Mo_2TiC_2 was an excellent photocatalyst with prominent photocatalytic activity and superior stability.

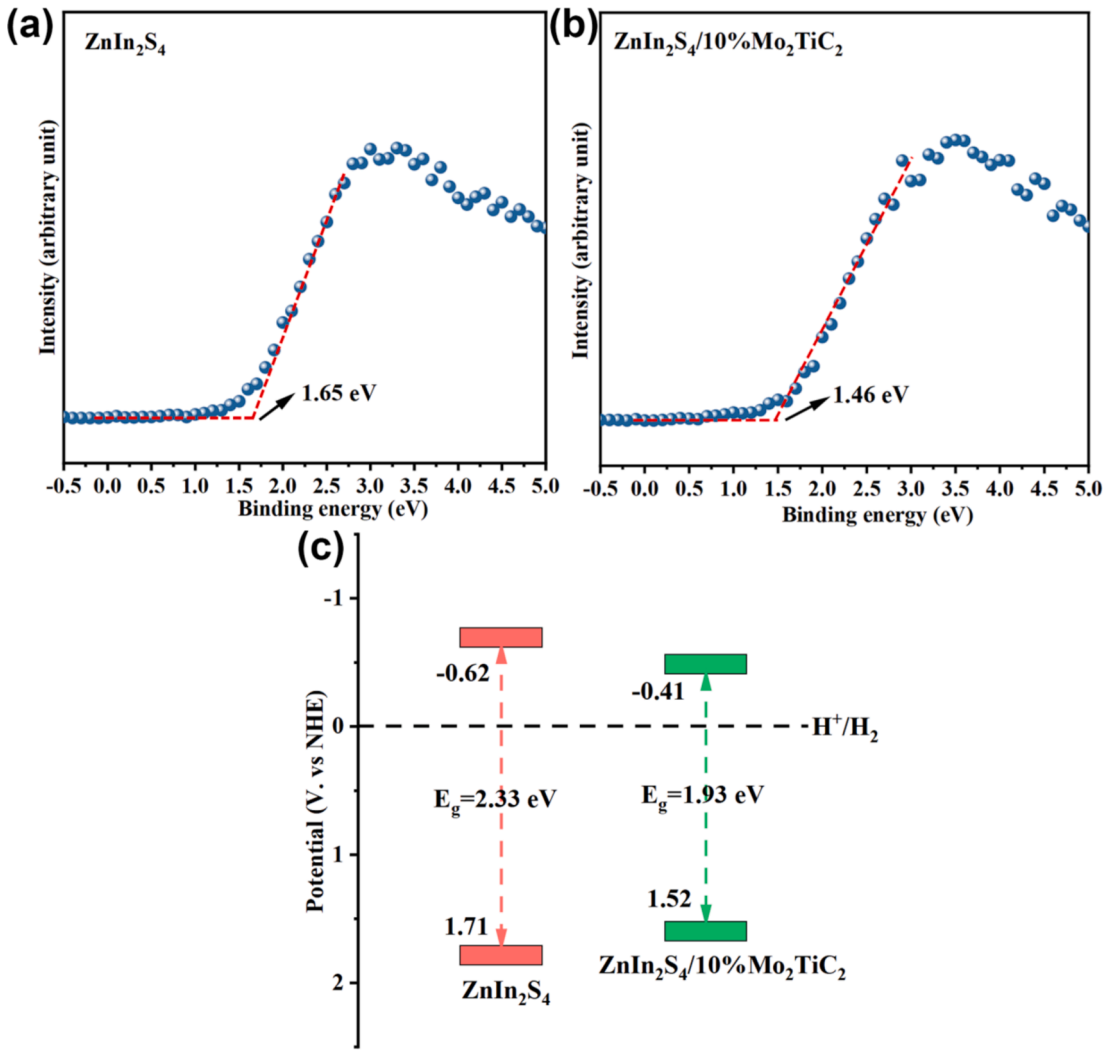

Fig. 6. Valence band XPS spectra of $ZnIn_2S_4$ (a) and $ZnIn_2S_4$/10 %Mo_2TiC_2 (b), (c) band structures of $ZnIn_2S_4$ and $ZnIn_2S_4$/10 %Mo_2TiC_2 .

3.3. *Photoelectrochemical property characterization*

In order to get insight into the improved photocatalytic hydrogen evolution performance of the catalysts, various characterizations were conducted on an electrochemical workstation to investigate charge carrier dynamics of the samples. As displayed in Fig. 5a, all $ZnIn_2S_4$/Mo_2TiC_2 binary composites showed obviously enhanced photocurrent response intensity compared to pristine $ZnIn_2S_4$, in the order $ZnIn_2S_4$/10 % Mo_2TiC_2 > $ZnIn_2S_4$/20 %Mo_2TiC_2 > $ZnIn_2S_4$/1 %Mo_2TiC_2 > $ZnIn_2S_4$, which was consistent with the order of the photocatalytic hydrogen evolution rate of the catalysts. Generally, the higher photocurrent response intensity meant the higher photogenerated charger carrier transfer efficiency, and it was clear that $ZnIn_2S_4$/10 %Mo_2TiC_2 exhibited the highest photocurrent response intensity among the samples, suggesting its most efficient photogenerated charge carrier transfer [60,61]. Moreover, the electrochemical impedance spectroscopy (EIS) of the samples was performed and the corresponding Randles circuit model was developed as shown in Fig. 5b, and the R_{ct}, R_s, Z_w and CPE represented the charge-transfer resistance, bulk solution resistance, Warburg impedance and double-layer capacitance, respectively [56]. It was evident that $ZnIn_2S_4$/10 %Mo_2TiC_2 had the smallest semicircle among the samples, and the charge-transfer resistance (R_{ct}) of $ZnIn_2S_4$/10 %Mo_2TiC_2 was determined to be 152.9 Ω, obviously smaller than that of pristine $ZnIn_2S_4$ (283.2 Ω), as detailed in Table S4. Consequently, it could be concluded that $ZnIn_2S_4$/10 %Mo_2TiC_2 possessed a reduced charge-transfer resistance and an improved photogenerated charge carrier transfer efficiency, as a result of the formation of electrons transfer path in the heterostructure [62].

The photoluminescence (PL) results in Fig. 5c implied that the emission peak intensity of the binary composites decreased significantly with the introduction of Mo_2TiC_2, and $ZnIn_2S_4$/10 %Mo_2TiC_2 exhibited the lowest PL emission intensity among the catalysts, indicating its suppressed charge carrier recombination [63], and it could be noticed that the emission peak of $ZnIn_2S_4$/20 %Mo_2TiC_2 was wider obviously, which mainly attributed to the effect of Mo_2TiC_2. Meanwhile, the fluorescence lifetime of $ZnIn_2S_4$/10 %Mo_2TiC_2 was calculated to be 6.65 ns based on the time-resolved photoluminescence (TRPL) results in Fig. 5d, which was longer than that of pure $ZnIn_2S_4$ (5.77 ns), jointly confirmed the accelerated interfacial charge carrier separation and transfer in the binary composite [64]. At the same time, the fluorescence lifetime of $ZnIn_2S_4$/20 %Mo_2TiC_2 was longer than that of $ZnIn_2S_4$/1 %Mo_2TiC_2 as shown in Fig. S11, which was also in good agreement with their photocatalytic hydrogen evolution performance. Additionally, the electron spin resonance (ESR) of pristine $ZnIn_2S_4$ and $ZnIn_2S_4$/10 %Mo_2TiC_2 was conducted to further elucidate the charge transport process in the catalysts, with TEMPO as trapping agent. As displayed in Fig. 5e, the TEMPO signal intensities of both samples were almost equal in the dark. While under light irradiation, both signals became weaker obviously (Fig. 5f), this was because TEMPO was consumed by the photogenerated electrons of the samples [26]. And it was worth noting that the signal

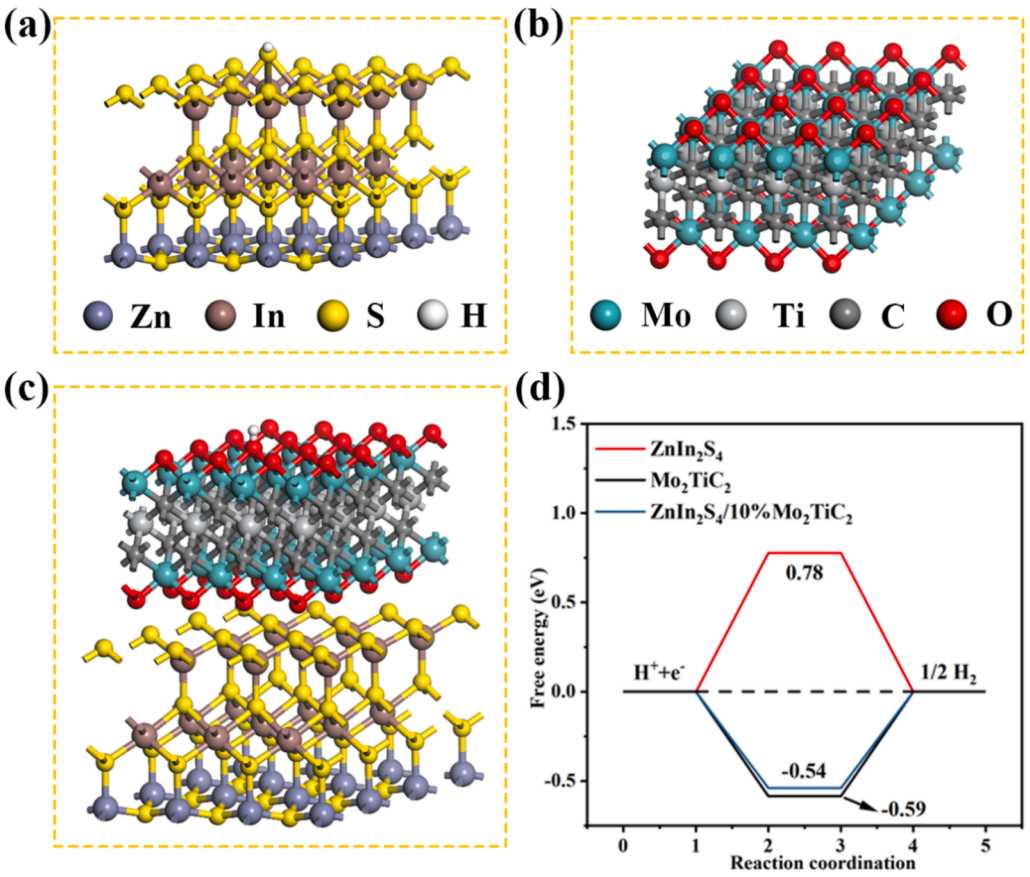

Fig. 7. Schematic structure models of H adsorption of $ZnIn_2S_4$ (a), Mo_2TiC_2 (b), and $ZnIn_2S_4$/10 %Mo_2TiC_2 (c), (d) free energy diagram of reaction coordinates on the prepared samples.

over $ZnIn_2S_4$/10 %Mo_2TiC_2 was much weaker than that of $ZnIn_2S_4$ under light irradiation, implying the higher concentration of photogenerated electrons in $ZnIn_2S_4$/10 %Mo_2TiC_2, which could be attributed to the improved charge separation efficiency facilitated by the introduction of Mo_2TiC_2. Besides, the surface photovoltage (SPV) spectra were analyzed to further confirm the photoelectric dynamic of the catalysts [65], as depicted in Fig. S12, both $ZnIn_2S_4$ and $ZnIn_2S_4$/10 % Mo_2TiC_2 exhibited obvious signal at the range of 300–600 nm, which illustrated that the most photogenerated electrons derived from interband transition [66]. And the signal intensity of $ZnIn_2S_4$/10 % Mo_2TiC_2 was obviously lower than that of pristine $ZnIn_2S_4$, the decreased signal intensity of $ZnIn_2S_4$/10 %Mo_2TiC_2 was attributed to the capture of the produced electrons by Mo_2TiC_2, resulting in less charge available for transport between the FTO electrodes of the SPV apparatus [67–69]. Those results confirmed that the introduced Mo_2TiC_2 could trap the photogenerated charge carriers in $ZnIn_2S_4$ and provide a more efficient pathway for charge carrier transfer, thereby reducing the recombination rate of photogenerated charge carriers and enhancing the photocatalytic performance of $ZnIn_2S_4$/10 %Mo_2TiC_2 composite. At the same time, the tightly-bound interface between $ZnIn_2S_4$ and Mo_2TiC_2 also contributed to the accelerated electrons transfer in the Schottky heterojunction.

3.4. Photocatalytic mechanism

The valence band potential (E_{VB}) of the samples was evaluated by VB-XPS, and the results were described in Fig. 6a-b. Based on the formula: $E_{VB} = \Phi + E_{VB,\ XPS}$-4.44, in which Φ was the work function of the analyzer (4.5 eV), the E_{VB} of $ZnIn_2S_4$ and $ZnIn_2S_4$/10 %Mo_2TiC_2 were calculated to be 1.71 and 1.52 V. Moreover, the band gap energies (E_g) of $ZnIn_2S_4$ and $ZnIn_2S_4$/10 %Mo_2TiC_2 were determined to be 2.33 and 1.93 eV from UV–Vis. DRS analysis. Consequently, the corresponding conduction band potential (E_{CB}) were calculated to be −0.62 and −0.41 V using the formula: $E_g = E_{VB}$-E_{CB}. As a result, the band position of the samples was summarized and depicted in Fig. 6c.

To explore the mechanism of the optimized photocatalytic performance of the binary composites, DFT calculation was conducted using the Perdew-Burke-Ernzerhof (PBE) formulation. As depicted in Fig. 7a-c, the fitted structure models of H adsorption over the samples were established, and the corresponding Gibbs free energy was calculated as shown in Fig. 7d, it could be noticed that the Gibbs free energy of $ZnIn_2S_4$/10 %Mo_2TiC_2 was obviously lower than those of Mo_2TiC_2 and $ZnIn_2S_4$. Generally, as for the photocatalytic hydrogen evolution process, a lower Gibbs free energy meant the reduced overpotential requirement [70], which was the extra voltage needed to drive the reaction beyond its theoretical minimum. And the reduced overpotential was beneficial for accelerating the photocatalytic hydrogen evolution rate. As a result, it could be concluded that the reaction barrier over $ZnIn_2S_4$/10 %Mo_2TiC_2 was smaller than those of Mo_2TiC_2 and $ZnIn_2S_4$, which was consistent with its enhanced photocatalytic performance.

The charge carrier behavior at the interface of Mo_2TiC_2 and $ZnIn_2S_4$ was investigated by calculating the Fermi energy level (E_f), using the formular: $E_f = E_{vac}$-Φ, where the E_{vac} was the energy of the vacuum energy level and Φ was the work function, which was defined as the minimum energy required to remove an electron from the surface of a sample into the vacuum energy level [71]. It was calculated that the work function of the pristine $ZnIn_2S_4$ (5.96 eV) was lower than that of Mo_2TiC_2 (7.43 eV) (Fig. 8a-b), resulting in a lower E_f of Mo_2TiC_2 compared to that of $ZnIn_2S_4$ This result also indicated that $ZnIn_2S_4$ was more prone to lose electrons than Mo_2TiC_2. As a result, due to the

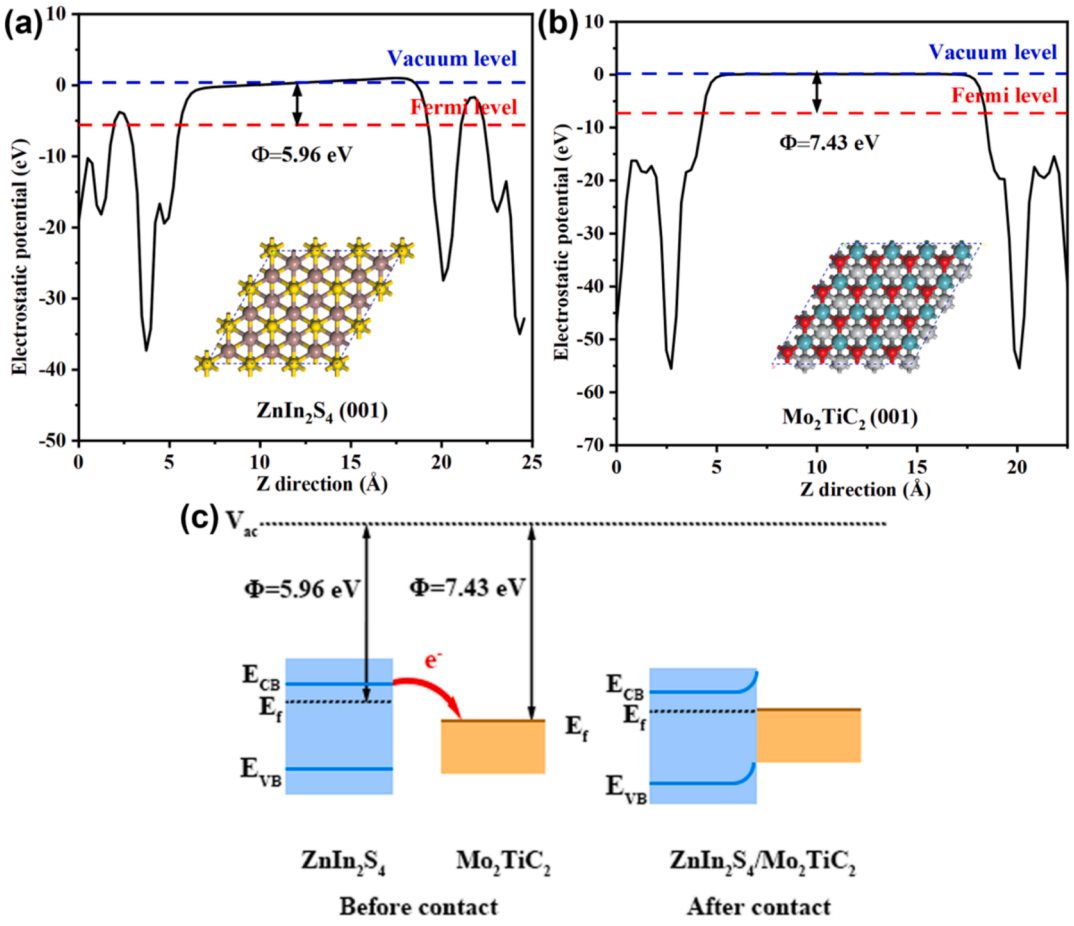

Fig. 8. Electrostatic potential of $ZnIn_2S_4$ (a) and Mo_2TiC_2 (b), (c) schematic illustration of the formation of $ZnIn_2S_4$/10 %Mo_2TiC_2 Schottky junction.

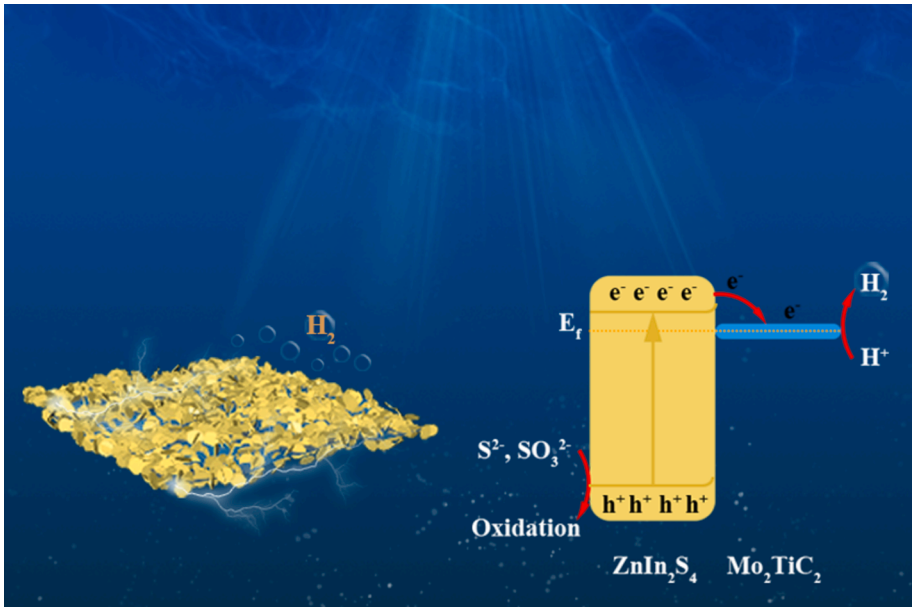

Fig. 9. Schematic illustration of the photocatalytic H_2 evolution mechanism of $ZnIn_2S_4$/10 %Mo_2TiC_2 Schottky junction.

different E_f between Mo_2TiC_2 and $ZnIn_2S_4$, the electrons would transfer through the tightly-bound interface and accumulate on the Mo_2TiC_2 side until reaching the E_f equilibrium, as described in Fig. 8c. And the band position of $ZnIn_2S_4$ would bend upward after contacting with Mo_2TiC_2, which could inhibit the electrons backflow effectively, implying the formation of the Schottky junction in the composite. Furthermore, the charge density difference analysis was conducted to explore the distribution of electrons density and the electrons transfer direction within the $ZnIn_2S_4$/10 %Mo_2TiC_2 heterostructure, as shown in Fig. S13a-b. The significant changes in electrons distribution at the interface of $ZnIn_2S_4$

and Mo_2TiC_2 could be clearly observed, and the electrons tended to accumulate on the Mo_2TiC_2 side (the yellow region), while the electrons deficient region (the cyan region) was almost centered on the $ZnIn_2S_4$ side. Additionally, the quantitative analysis result illustrated that each Mo_2TiC_2 unit gained about 0.30 electrons from $ZnIn_2S_4$, firmly demonstrating that the electrons transferred from $ZnIn_2S_4$ to Mo_2TiC_2 across the interface in the composites.

Based on the above results including in situ XPS, Fermi energy level and electrons density difference calculation results, the Schottky heterojunction photocatalytic mechanism could be proposed as shown in Fig. 9. Specifically, the electrons would be excited from VB to CB of $ZnIn_2S_4$ under simulated sunlight irradiation, then transfer to the surface of Mo_2TiC_2 and reduce the absorbed protons to H_2. At the same time, the photogenerated holes left in VB of $ZnIn_2S_4$ would be consumed by the added sacrificial agents, and it was worth noting that the upward bending of band position of $ZnIn_2S_4$ could effectively inhibit the electrons backflow. In this way, the photogenerated charge carrier separation and transfer efficiency of $ZnIn_2S_4/Mo_2TiC_2$ composites could be improved, which accounted for the accelerated photocatalytic hydrogen evolution performance. In summary, the incorporation of Mo_2TiC_2 allowed for the capture of photogenerated electrons and provided a shorter electron transfer pathway by tightly integrating with $ZnIn_2S_4$, significantly reduced the charge carrier recombination and boosted the photocatalytic activity of the composites.

4. Conclusion

In summary, a novel $ZnIn_2S_4/Mo_2TiC_2$ Schottky heterojunction with strong interfacial interaction was successfully constructed via in situ growth of $ZnIn_2S_4$ nanosheets on the surface of few-layered Mo_2TiC_2 MXene. The in situ XPS and DFT calculations illustrated that photoproduced electrons transferred from $ZnIn_2S_4$ to Mo_2TiC_2 MXene across the tightly-bound interface, due to the difference of the Fermi levels. Besides, the formation of Schottky junction with strong interfacial interaction effectively facilitated the charge carrier transfer and inhibited the backflow of the electrons, thereby significantly enhanced the PHE rate of the binary composites. Additionally, $ZnIn_2S_4/Mo_2TiC_2$ binary composites exhibited improved optical properties compared to pure $ZnIn_2S_4$, owing to the excellent light absorption ability of Mo_2TiC_2 MXene. As expected, $ZnIn_2S_4$/10 %Mo_2TiC_2 achieved the highest hydrogen production rate of 4.3 $mmol \cdot g^{-1} \cdot h^{-1}$ (using 10 mg of catalyst), without the use of any noble-metal co-catalyst. This rate was approximately 3.8 times greater than that of pristine $ZnIn_2S_4$ and also exceeded the rates observed for $ZnIn_2S_4$ with 10 %Ti_3C_2 or 1 %Pt as co-catalysts. This work put forward an optimized strategy for synthesizing few-layered Mo_2TiC_2 MXene with a large lamellar structure and convinced its potential in fabricating the high-performance Mo_2TiC_2-based photocatalysts as an excellent platform material.

CRediT authorship contribution statement

Huihui Zhang: Conceptualization, Methodology, Validation, Investigation, Writing – original draft. **Yamei Huang:** Writing – review & editing. **Xinglin Wang:** Validation, Formal analysis. **Jiayi Meng:** Validation. **Linlin Gao:** Formal analysis. **Yu Li:** Formal analysis. **Yu Zhang:** Validation. **Yifan Liao:** Formal analysis. **Wei-Lin Dai:** Funding acquisition, Project administration, Supervision, Writing – review & editing, Visualization.

Declaration of competing interest

The authors declare that they have no known competing financial interests or personal relationships that could have appeared to influence the work reported in this paper.

Acknowledgments

This work was financially supported by the National Key Research and Development Program of China (2021YFA1501404), Natural Science Foundation of Shanghai (22ZR1404200), and Natural Science Foundation of Shanghai Science and Technology Committee (19DZ2270100).

Appendix A. Supplementary data

Supplementary data to this article can be found online at https://doi.org/10.1016/j.seppur.2024.131199.

Data availability

Data will be made available on request.

References

[1] J. Pan, D. Wang, B. Zhang, C. Zhao, D. Liu, S. Liu, Z. Zeng, T. Chen, G. Liu, S. Jiao, Z. Xu, T. Liu, T. Liu, X. Fang, L. Zhao, J. Wang, Atomic-level charge separation boosting the photocatalytic hydrogen evolution, Chem. Eng. J. 487 (2024) 150536.
[2] J. Li, J. Jia, D. Wang, H. Dong, M. Zhu, Recent research progress of MOFs-based heterostructures for photocatalytic hydrogen evolution, Chem. Eng. J. 498 (2024) 155194.
[3] D. Ma, J. Chen, J. Li, X. Ji, J.-W. Shi, A review on passivation engineering for improving photocatalytic hydrogen evolution performance, J. Mater. Chem. A 12 (2024) 12293–12324.
[4] A. Fujishima, K. Honda, Electrochemical photolysis of water at a semiconductor electrode, Nature 238 (1972) 37–38.
[5] Q. Zhang, J. Zhang, X. Wang, L. Li, Y.-F. Li, W.-L. Dai, In-N-In sites boosting interfacial charge transfer in carbon-coated hollow tubular $In_2O_3/ZnIn_2S_4$ heterostructure derived from In-MOF for enhanced photocatalytic hydrogen evolution, ACS Catal. 11 (2021) 6276–6289.
[6] B. Liu, Y. Li, Y. Guo, Y. Tang, C. Wang, Y. Sun, X. Tan, Z. Hu, T. Yu, Regulating the transfer of photogenerated carriers for photocatalytic hydrogen evolution coupled with furfural synthesis, ACS Nano 18 (2024) 17939–17949.
[7] E.N. Musa, A.K. Yadav, K.T. Smith, M.S. Jung, W.F. Stickle, P. Eschbach, X. Ji, K. Stylianou, Boosting photocatalytic hydrogen production by MOF-derived metal oxide heterojunctions with a 10.0 % apparent quantum yield, Angew. Chem. Int. Ed. 63 (2024) e202405681.
[8] X. Wang, L. Li, H. Gu, H. Zhang, J. Zhang, Q. Zhang, W.-L. Dai, Highly efficient noble-metal-free NiS/rGO/$Cd_{0.3}Zn_{0.7}S$ nanorods in visible-light-driven H_2 evolution with enhanced surface photoinduced charge transfer, Appl. Surf. Sci. 574 (2022) 151553.
[9] J. Zhang, H. Gu, X. Wang, H. Zhang, S. Chang, Q. Li, W.-L. Dai, Robust S-scheme hierarchical Au-$ZnIn_2S_4/NaTaO_3$: facile synthesis, superior photocatalytic H_2 production and its charge transfer mechanism, J. Colloid Interface Sci. 625 (2022) 785–799.
[10] F. Wu, X. Zhang, L. Wang, G. Li, J. Huang, A. Song, A. Meng, Z. Li, Enhanced spin-polarized electric field modulating p-band center on Ni-doped CdS for boosting photocatalytic hydrogen evolution, Small 20 (2024) 2309439.
[11] M. Ding, S. Cui, Z. Lin, X. Yang, Crystal facet engineering of hollow cadmium sulfide for efficient photocatalytic hydrogen evolution, Appl. Catal. B 357 (2024) 124333.
[12] L. Li, X. Wang, H. Gu, H. Zhang, J. Zhang, Q. Zhang, W.-L. Dai, Which is more efficient in promoting the photocatalytic H_2 evolution performance of g-C_3N_4: monometallic nanocrystal, heterostructural nanocrystal, or bimetallic nanocrystal? Inorg. Chem. 61 (2022) 4760–4768.
[13] Y. Zhang, X. Ran, H. Fu, Y. Gong, S. Li, F. Gu, S. Wang, X. An, D. Su, X. Yang, Band alignment tunning via the facets of CdS nanocrystals with g-C_3N_4 for unveiling their enhanced photocatalytical property, Adv. Funct. Mater. 34 (2024) 2404585.
[14] D. Jang, S. Lee, N.H. Kwon, T. Kim, S. Park, K.Y. Jang, E. Yoon, S. Choi, J. Han, T.-W. Lee, J. Kim, S.-J. Hwang, S. Park, Preparation of carbon nitride nanotubes with P-doping and their photocatalytic properties for hydrogen evolution, Carbon 208 (2023) 290–302.
[15] H. Zhang, H. Gu, X. Wang, L. Li, J. Zhang, S. Chang, W.-L. Dai, Embedding indium nitride at the interface of indium-oxide/indium-zinc-sulfide heterostructure with enhanced interfacial charge transfer for high photocatalytic hydrogen evolution, J. Colloid Interface Sci. 622 (2022) 539–548.
[16] C. Li, H. Liang, Z. Xu, J. Tao, Y. Zhang, K. Dong, L.-L. Wang, L. Xu, Construction of Z-scheme InN/BTe heterostructure for enhanced photocatalytic hydrogen evolution: DFT calculation and mechanism study, Int. J. Hydrogen Energy 68 (2024) 289–296.
[17] H. Gu, H. Zhang, X. Wang, Q. Li, S. Chang, Y. Huang, L. Gao, Y. Cui, R. Liu, W.-L. Dai, Robust construction of CdSe nanorods@Ti_3C_2 MXene nanosheet for superior photocatalytic H_2 evolution, Appl. Catal. B 328 (2023) 122537.
[18] X. Chen, Y. Guo, J. Li, H. Yang, Z. Chen, D. Luo, X. Liu, Elemental doping tailoring photocatalytic hydrogen evolution of InP/ZnSeS/ZnS quantum dots, Chem. Eng. J. 496 (2024) 153947.

[19] Z. Fan, X. Guo, M. Yang, Z. Jin, Mechanochemical preparation and application of graphdiyne coupled with CdSe nanoparticles for efficient photocatalytic hydrogen production, Chin. J. Catal. 43 (2022) 2708–2719.

[20] M. Cao, F. Yang, Q. Zhang, J. Zhang, L. Zhang, L. Li, X. Wang, W.-L. Dai, Facile construction of highly efficient MOF-based Pd@UiO-66-NH_2@$ZnIn_2S_4$ flower-like nanocomposites for visible-light-driven photocatalytic hydrogen production, J. Mater. Sci. Technol. 76 (2021) 189–199.

[21] Y. Zhang, D. Ma, J. Li, C. Zhi, Y. Zhang, L. Liang, S. Mao, J.-W. Shi, Recent research advances of metal organic frameworks (MOFs) based composites for photocatalytic H_2 evolution, Coord. Chem. Rev. 517 (2024) 215995.

[22] T.K. Saothayanun, Y. Inchongkol, N. Weeranoppanant, M. Kondo, M. Ogawa, S. Bureekaew, Self-shuttle-mediated electron transfer to boost photocatalytic hydrogen production of Co-Zn bimetallic MOF, J. Mater. Chem. A 12 (2024) 26743–26748.

[23] S. Qi, K. Zhu, T. Xu, H. Zhang, X. Guo, J. Wang, F. Zhang, X. Zong, Water-stable high-entropy metal-organic framework nanosheets for photocatalytic hydrogen production, Adv. Mater. 36 (2024) 2403328.

[24] S. Jiang, H. Niu, Q. Sun, R. Zhao, N. Li, Y. Cai, Significant improvement of photocatalytic hydrogen evolution performance in covalent organic frameworks: substituent fine-tuning, J. Mater. Chem. A 12 (2024) 11416–11423.

[25] N. Liu, S. Xie, Y. Huang, J. Lu, H. Shi, S. Xu, G. Zhang, X. Chen, Dual-acceptor engineering in pyrene-based covalent organic frameworks for boosting photocatalytic hydrogen evolution, Adv. Energy Mater. 14 (2024) 2402395.

[26] Q. Zhang, H. Gu, X. Wang, L. Li, J. Zhang, H. Zhang, Y.-F. Li, W.-L. Dai, Robust hollow tubular $ZnIn_2S_4$ modified with embedded metal-organic-framework-layers: extraordinarily high photocatalytic hydrogen evolution activity under simulated and real sunlight irradiation, Appl. Catal. B 298 (2021) 120632.

[27] S. Wang, D. Zhang, X. Pu, L. Zhang, D. Zhang, J. Jiang, Photothermal-enhanced S-scheme heterojunction of hollow core-shell $FeNi_2S_4$@$ZnIn_2S_4$ toward photocatalytic hydrogen evolution, Small 20 (2024) 2311504.

[28] T. Xiao, L. Wang, K. Li, J. Tang, R. Du, S. Rao, M. Wu, Donor-acceptor-donor organic small molecules as hole transfer vehicle covalently coupled $ZnIn_2S_4$ nanosheets for efficient photocatalytic hydrogen evolution, Adv. Funct. Mater. (2024) 2412644.

[29] B. Sun, J. Bu, Y. Du, X. Chen, Z. Li, W. Zhou, O, S-dual-vacancy defects mediated efficient charge separation in $ZnIn_2S_4$/black TiO_2 heterojunction hollow spheres for boosting photocatalytic hydrogen production, ACS Appl. Mater. Interfaces 13 (2021) 37545–37552.

[30] M. Xu, X. Ruan, D. Meng, G. Fang, D. Jiao, S. Zhao, Z. Liu, Z. Jiang, K. Ba, T. Xie, W. Zhang, J. Leng, S. Jin, S.K. Ravi, X. Cui, Modulation of sulfur vacancies in $ZnIn_2S_4$/MXene Schottky heterojunction photocatalyst promotes hydrogen evolution, Adv. Funct. Mater. 34 (2024) 2402330.

[31] W. Guan, L. Zhang, P. Wang, Y. Wang, H. Wang, X. Dong, L. Yu, Z. Gan, L. Dong, L. Sui, Efficient photocatalytic hydrogen evolution based on a Z-scheme 2D $LaVO_4$/2D Mo-doped S_V-$ZnIn_2S_4$ heterojunction, J. Mater. Chem. A 12 (2024) 12181–12189.

[32] L. Jia, N. Ma, P. Shao, Y. Ge, J. Liu, W. Dong, H. Song, C. Lu, Y. Zhou, X. Xu, Incorporating ReS_2 nanosheet into $ZnIn_2S_4$ nanoflower as synergistic Z-scheme photocatalyst for highly effective and stable visible-light-driven photocatalytic hydrogen evolution and degradation, Small (2024) 2404622.

[33] P. Bhavani, M.R. Ashwin Kishore, D. Praveen Kumar, J.S. Yoo, Y.-K. Park, Enhanced solar to hydrogen conversion via Ni addition to a few layered 2D/2D g-C_3N_4/$ZnIn_2S_4$ heterojunction, J. Mater. Chem. A 12 (2024) 16546–16558.

[34] Z. Bao, Y. Jiang, Z. Zhang, J. Lv, W. Shen, J. Dai, J. Wang, J. Cai, Y. Wu, Visible-light-responsive S-vacancy $ZnIn_2S_4$/N-doped TiO_2 nanoarray heterojunctions for high-performance photoelectrochemical water splitting, J. Mater. Chem. A 12 (2024) 15902–15913.

[35] P. Lu, K. Liu, Y. Liu, Z. Ji, X. Wang, B. Hui, Y. Zhu, D. Yang, L. Jiang, Heterostructure with tightly-bound interface between In_2O_3 hollow fiber and $ZnIn_2S_4$ nanosheet toward efficient visible light driven hydrogen evolution, Appl. Catal. B 345 (2024) 123697.

[36] M. Geng, X. Wang, S. Yuan, T. Zhao, J. Zhang, L. Wang, Z. Liu, M. Sun, G. Yin, Synthesis of ternary MoS_2/carbon dots/$ZnIn_2S_4$ nanocomposites for enhanced photocatalytic hydrogen evolution, Energy Fuels 38 (2024) 8124–8133.

[37] X.-L. Li, X.-J. Wang, J.-Y. Zhu, Y.-P. Li, J. Zhao, F.-T. Li, Fabrication of two-dimensional Ni_2P/$ZnIn_2S_4$ heterostructures for enhanced photocatalytic hydrogen evolution, Chem. Eng. J. 353 (2018) 15–24.

[38] S. Yuan, G. Liu, Q. Zhang, T. Liu, J. Yang, Z. Guan, Synergistic effect of Na doping and $CoSe_2$ cocatalyst for enhanced photocatalytic hydrogen evolution performance of $ZnIn_2S_4$, J. Colloid Interface Sci. 676 (2024) 272–282.

[39] I. Ali, M. Yousaf, I.H. Sajid, M.W. Hakim, S. Rizwan, Reticulation of 1D/2D Mo_2TiC_2 MXene for excellent supercapacitor performance, Mater. Today Chem. 34 (2023) 101766.

[40] P.A. Maughan, L. Bouscarrat, V.R. Seymour, S. Shao, S.J. Haigh, R. Dawson, N. Tapia-Ruiz, N. Bimbo, Pillared Mo_2TiC_2 MXene for high-powder and long-life lithium and sodium-ion batteries, Nanoscale Adv. 3 (2021) 3145–3158.

[41] S. Delgado, Y. Remedios-Díaz, J.C. Calderón, S. Díaz-Coello, M.C. Arévalo, G. García, E. Pastor, Catalytic activity of 2D MXenes toward electroreduction processes: oxygen reduction and hydrogen evolution reactions, Int. J. Hydrogen Energy 55 (2024) 1050–1061.

[42] L.-H. Zheng, C.-K. Tang, Q.-F. Lü, J. Wu, MoS_2/$Mo_2TiC_2T_x$ supported Pd nanoparticles as an efficient electrocatalyst for hydrogen evolution reaction in both acidic and alkaline media, Int. J. Hydrogen Energy 47 (2022) 11739–11749.

[43] C.-K. Tang, X. Zheng, X.-L. Chen, Y.-G. Fu, Q.-F. Lü, Defect-rich MoS_2/CoS_2 on $Mo_2TiC_2T_x$ MXene as an efficient catalyst for hydrogen evolution reaction in acidic media, FlatChem 42 (2023) 100581.

[44] X. Zhao, K. Tang, C. Lee, C.F. Du, H. Yu, X. Wang, W. Qi, Q. Ye, Q. Yan, Promoting the water-reduction kinetics and alkali tolerance of $MoNi_4$ nanocrystals via a $Mo_2TiC_2T_x$ induced built-in electric field, Small 18 (2022) 2107541.

[45] Q. Xi, F. Xie, J. Liu, X. Zhang, J. Wang, Y. Wang, W. Wang, H. Li, Z. Yu, Z. Sun, X. Jian, X. Gao, J. Ren, C. Fan, R. Li, In situ formation $ZnIn_2S_4$/Mo_2TiC_2 Schottky junction for accelerating photocatalytic hydrogen evolution kinetics: manipulation of local coordination and electronic structure, Small 19 (2023) 2300717.

[46] Q. Xi, J. Liu, F. Xie, A. Jian, Z. Sun, A. Zhou, X. Jian, X. Zhang, Y. Wang, H. Li, X. Gao, J. Ren, C. Fan, J. Wang, R. Li, Electron-parking engineering assisted $ZnIn_2S_4$/Mo_2TiC_2-Ru photocatalytic hydrogen evolution for efficient solar energy conversion and storage, Appl. Catal. B 355 (2024) 124184.

[47] Y. Fan, X. Hao, N. Yi, Z. Jin, Strong electronic coupling of Mo_2TiC_2 MXene/ZnCdS ohmic junction for boosting photocatalytic hydrogen evolution, Appl. Catal. B 357 (2024) 124313.

[48] G. Zuo, Y. Wang, W.L. Teo, A. Xie, Y. Guo, Y. Dai, W. Zhou, D. Jana, Q. Xian, W. Dong, Y. Zhao, Ultrathin $ZnIn_2S_4$ nanosheets anchored on $Ti_3C_2T_X$ MXene for photocatalytic H_2 evolution, Angew. Chem. Int. Ed. 59 (2020) 11287–11292.

[49] Y. Chen, Y. Ge, C. Wu, H. Tang, X. Luo, J. He, L. Jiang, Z. Yan, J. Wang, Facile synthesis of 2D/2D Ti_3C_2/$ZnIn_2S_4$ heterostructure for enhanced photocatalytic hydrogen generation, Int. J. Mol. Sci. 24 (2023) 3936.

[50] W. Huang, Z. Li, C. Wu, H. Zhang, J. Sun, Q. Li, Delaminating Ti_3C_2 MXene by blossom of $ZnIn_2S_4$ microflowers for noble-metal-free photocatalytic hydrogen production, J. Mater. Sci. Technol. 120 (2022) 89–98.

[51] M. Du, L. Li, S. Ji, T. Wang, Y. Wang, J. Zhang, X.a. Li, In situ growth of 2D $ZnIn_2S_4$ nanosheets on sulfur-doped porous $Ti_3C_2T_x$ MXene 3D multi-functional architectures for photocatalytic H_2 evolution, J. Mater. Chem. C 10 (2022) 10636–10644.

[52] F. Hu, X. Wang, S. Bao, L. Song, S. Zhang, H. Niu, B. Fan, R. Zhang, H. Li, Tailoring electromagnetic responses of delaminated $Mo_2TiC_2T_x$ MXene through the decoration of Ni particles of different morphologies, Chem. Eng. J. 440 (2022) 135855.

[53] F. Hu, X. Wang, H. Niu, S. Zhang, B. Fan, R. Zhang, Synthesis and electromagnetic wave absorption of novel $Mo_2TiC_2T_x$ MXene with diverse etching methods, J. Mater. Sci. 57 (2022) 7849–7862.

[54] M. Tan, Y. Ma, C. Yu, Q. Luan, J. Li, C. Liu, W. Dong, Y. Su, L. Qiao, L. Gao, Q. Lu, Y. Bai, Boosting photocatalytic hydrogen production via interfacial engineering on 2D ultrathin Z-Scheme $ZnIn_2S_4$/g-C_3N_4 heterojunction, Adv. Funct. Mater. 32 (2022) 2111740.

[55] H. Zhang, H. Gu, Y. Huang, X. Wang, L. Gao, Q. Li, Y. Li, Y. Zhang, Y. Cui, R. Gao, W.-L. Dai, Rational design of covalent organic frameworks/$NaTaO_3$ S-scheme heterostructure for enhanced photocatalytic hydrogen evolution, J. Colloid Interface Sci. 664 (2024) 916–927.

[56] H. Zhang, H. Gu, X. Wang, S. Chang, Q. Li, W.-L. Dai, Fabrication of noble-metal-free hierarchical rectangular tubular S-scheme NiS/$ZnIn_2S_4$/$AgIn(WO_4)_2$ nanocomposite for highly efficient photocatalytic hydrogen evolution, Chem. Eng. J. 457 (2023) 141185.

[57] Q. Zhao, W. Zhou, M. Zhang, Y. Wang, Z. Duan, C. Tan, B. Liu, F. Ouyang, Z. Yuan, H. Tai, Y. Jiang, Edge-enriched $Mo_2TiC_2T_x$/MoS_2 heterostructure with coupling interface for selective NO_2 monitoring, Adv. Funct. Mater. 32 (2022) 2203528.

[58] J.-Y. Li, Y.-H. Li, F. Zhang, Z.-R. Tang, Y.-J. Xu, Visible-light-driven integrated organic synthesis and hydrogen evolution over 1D/2D CdS-$Ti_3C_2T_x$ MXene composites, Appl. Catal. B 269 (2020) 118783.

[59] H.-B. Huang, Z.-B. Fang, K. Yu, J. Lü, R. Cao, Visible-light-driven photocatalytic H_2 evolution over CdZnS nanocrystal solid solutions: interplay of twin structures, sulfur vacancies and sacrificial agents, J. Mater. Chem. A 8 (2020) 3882–3891.

[60] C.-J. Lu, W.-J. Shi, Y.-N. Gong, J.-H. Zhang, Y.-C. Wang, J.-H. Mei, Z.-M. Ge, T.-B. Lu, D.-C. Zhong, Modulating the microenvironments of robust metal hydrogen-bonded organic frameworks for boosting photocatalytic hydrogen evolution, Angew. Chem. Int. Ed. 63 (2024) e202405451.

[61] F. Huang, Z. Li, Y. Xu, A. Yan, T. Zhang, Q. Wang, S. Li, S. Lu, W. Zhao, Y. Gao, J. Zhang, Excellent anti-photocorrosion and hydrogen evolution activity of $ZnIn_2S_4$-based photocatalysts: in-situ design of photogenerated charge dynamics, Chem. Eng. J. 473 (2023) 145430.

[62] X. Dai, S. Feng, W. Wu, Y. Zhou, Z. Ye, X. Cao, Y. Wang, C. Yang, Photocatalytic hydrogen evolution and antibiotic degradation by S-scheme $ZnCo_2S_4$/TiO_2, Int. J. Hydrogen Energy 47 (2022) 25104–25116.

[63] H. Zhao, R. Greco, H.-P. Komsa, R. Sliz, O. Pitkänen, K. Kordas, S. Ojala, 1 T′/2 H MoS_2 nanoflowers integrated with bismuth halide perovskite for improved photocatalytic hydrogen evolution, Appl. Catal. B 357 (2024) 124318.

[64] S. Gao, B. Wang, F. Chen, G. He, T. Zhang, L. Li, J. Li, Y. Zhou, B. Feng, D. Mei, J. Yu, Confinement of $CsPbBr_3$ perovskite nanocrystals into extra-large-pore zeolite for efficient and stable photocatalytic hydrogen evolution, Angew. Chem. Int. Ed. 63 (2024) e202319996.

[65] A. Yan, T. Zhang, F. Huang, S. Lu, Q. Wang, H. Yuan, Y. Gao, W. Zhao, J. Zhang, Z. Su, *In situ* construction of Ohmic/Schottky-type MoS_2/S_v-$ZnIn_2S_4/Cu(OH)_2$ dual-junction photocatalysts with enhanced water splitting into hydrogen generation activity, J. Mater. Chem. A 12 (2024) 14646.
[66] X. Kong, F. Lv, H. Zhang, F. Yu, Y. Wang, L. Yin, J. Huang, Q. Feng, NiO load $K_2Fe_4O_7$ enhanced photocatalytic hydrogen production and photo-generated carrier behavior, J. Alloys Compd. 903 (2022) 163864.
[67] S. Verbruggen, J. Dirckx, J. Martens, S. Lenaerts, Surface photovoltage measurements: a quick assessment of the photocatalytic activity? Catal. Today 209 (2013) 215–220.
[68] L. Jing, X. Sun, J. Shang, W. Cai, Z. Xu, Y. Du, H. Fu, Review of surface photovoltage spectra of nano-sized semiconductor and its applications in heterogeneous photocatalysis, Sol. Energy Mater. Sol. Cells 79 (2003) 133–151.
[69] B. Xin, Z. Ren, P. Wang, J. Liu, L. Jing, H. Fu, Study on the mechanisms of photoinduced carriers separation and recombination for Fe^{3+}-TiO_2 photocatalysts, Appl. Surf. Sci. 253 (2007) 4390–4395.
[70] H. Li, R. Li, Y. Jing, B. Liu, Q. Xu, T. Tan, G. Liu, L. Zheng, L.-Z. Wu, S-scheme heterojunction/single-atom dual-driven charge transport for photocatalytic hydrogen production, ACS Catal. 14 (2024) 7308–7320.
[71] T. Wang, X. Pan, M. He, L. Kang, W. Ma, In situ construction of hollow coral-like porous S-doped g-$C_3N_4/ZnIn_2S_4$ S-scheme heterojunction for efficient photocatalytic hydrogen evolution, Adv. Sci. 11 (2024) 2403771.